

## Influence of strain relaxation on the relative orientation of ZnO and ZnMnO wurtzite lattice with respect to sapphire substrates

This content has been downloaded from IOPscience. Please scroll down to see the full text.

2016 Mater. Res. Express 3 095902

(<http://iopscience.iop.org/2053-1591/3/9/095902>)

View [the table of contents for this issue](#), or go to the [journal homepage](#) for more

### Download details:

IP Address: 207.162.240.147

This content was downloaded on 05/09/2016 at 05:47

Please note that [terms and conditions apply](#).

You may also be interested in:

[Surface and interface engineering of ZnO based heterostructures fabricated by pulsed-laser deposition](#)

A Tsukazaki, A Ohtomo and M Kawasaki

[Polarity of oxide surfaces and nanostructures](#)

Jacek Goniakowski, Fabio Finocchi and Claudine Noguera

[ZnO epitaxial layers grown on c-sapphire substrate with MgO buffer](#)

M W Cho, A Setiawan, H J Ko et al.

[Low-dimensional systems investigated by x-ray absorption spectroscopy: a selection of 2D, 1D and 0D cases](#)

Lorenzo Mino, Giovanni Agostini, Elisa Borfecchia et al.

[Stress evolution during growth of GaN \(0001\)/Al<sub>2</sub>O<sub>3</sub>\(0001\) by reactive dc magnetron sputter epitaxy](#)

M Junaid, P Sandström, J Palisaitis et al.

[Growth and applications of Group III-nitrides](#)

O Ambacher

# Materials Research Express



## PAPER

# Influence of strain relaxation on the relative orientation of ZnO and ZnMnO wurtzite lattice with respect to sapphire substrates

RECEIVED  
2 September 2015

REVISED  
3 December 2015

ACCEPTED FOR PUBLICATION  
15 December 2015

PUBLISHED  
2 September 2016

K A Avramenko<sup>1</sup>, V P Bryksa<sup>1</sup>, T L Petrenko<sup>1</sup>, V P Kladko<sup>1</sup>, H V Stanchu<sup>1</sup>, A E Belyaev<sup>1</sup>, C Deparis<sup>2</sup>,  
J Zuñiga-Pérez<sup>2</sup> and C Morhain<sup>2</sup>

<sup>1</sup> V Lashkaryov Institute of Semiconductor Physics NASU, 45 Nauky pr., 03028 Kyiv, Ukraine

<sup>2</sup> Centre de Recherches sur l'Hétéro-Epitaxie et ses Applications (CRHEA), Centre National de la Recherche Scientifique (CNRS), Rue B. Gregory, F-06560 Valbonne Sophia Antipolis, France

**Keywords:** ZnO/sapphire interface, first-principle calculation, large lattice mismatch, Zn<sub>1-x</sub>Mn<sub>x</sub>O

## Abstract

ZnO and Zn<sub>1-x</sub>Mn<sub>x</sub>O ( $0 \leq x \leq 0.07$ ) films with 2 μm thickness were grown on (0001) sapphire substrate by molecular beam epitaxy. X-ray, electronic and optical studies show that films have a single crystalline columnar structure with unevenly distributed impurities and defects at the interfaces and boundaries of columns. ZnO and Zn<sub>1-x</sub>Mn<sub>x</sub>O films shows a high-quality hexagonal crystal structure with ZnO cells rotated by 30° relative to the sapphire substrate. We establish that the lateral coherence length obtained from x-ray analysis of Zn<sub>1-x</sub>Mn<sub>x</sub>O films is decreased from 900 nm to 400 nm at Mn variation from  $x = 0$  to 0.07, which corresponds to variation of an average column diameter in these films. We find that in Zn<sub>1-x</sub>Mn<sub>x</sub>O films the area sizes of coherent phonon decaying are determined by the coherent areas of concentration homogeneity of Mn distributions which are much smaller than the dimensions of the columns. Modeling of ZnO/Al<sub>2</sub>O<sub>3</sub> interface structure and properties was performed by means of first-principle density functional theory calculations. We employ an approach based on the use of large supercells (up to 460 atoms) which makes the simulation of interfaces with very large lattice mismatch possible. In this case amorphization of crystal structure in the vicinity of the interface is appears as a natural result of calculations leading to reduction of internal strains that that originate from the ZnO/Al<sub>2</sub>O<sub>3</sub> lattice mismatch. In all cases the double ZnO layer next closest to the to interface (as well as the upper layers) maintains a nearly perfect wurtzite crystal structure. Based on calculations we propose a new model of interface microstructure which includes Zn- or O-monolayers located between conventional ZnO and Al<sub>2</sub>O<sub>3</sub> surfaces. Adhesion energies of ZnO films to sapphire substrate were calculated for unrotated as well as for 30° rotated domains in the cases of Zn- and O-faced ZnO surfaces both with and without additional Zn- or O-monolayers. Comparison of these quantities suggests that energy gain at interface formation is somewhat larger for 30°- rotated domains than for unrotated ones.

## 1. Introduction

ZnO based wide-band gap semiconductors and corresponding solid solutions have attracted growing interest during the last decade owing to their great potential for optoelectronic and spintronic applications. Zn<sub>1-x</sub>Mn<sub>x</sub>O and Zn<sub>1-x</sub>Co<sub>x</sub>O magnetic films show appropriate physico-chemical properties and are technology-compatible with other semiconductors that are employed for chip fabrication. Promising materials for creation of light-emitting diodes [1], spin-polarized lasers [2], spin qubits for quantum computers [3] and nonvolatile magnetic semiconductor memory [4].

According to the p-d Zener model, Zn<sub>1-x</sub>Mn<sub>x</sub>O can be made ferromagnetic at room temperature, which is attractive for various applications in microelectronics, providing that the material may be doped *p*-type, as the ferromagnetic exchange between Mn ions should be mediated by holes. While in some papers the existence of high temperature magnetic ordering is called into question or its detection is complicated by the

antiferromagnetic ordering caused by existence of secondary uncontrolled structural phases, there are also claims that ferromagnetism was obtained in some samples, in which anomalous Hall effect [5] and high spin coherence with  $\tau_{\text{coh}} = 178 \mu\text{s}$  [3] were measured.

Structural investigations show that  $\text{Zn}_{1-x}\text{Mn}_x\text{O}$  magnetic films have complex mosaic and block microstructures with a large number of nonuniformly distributed defects and impurities. In this case magnetic ordering may be the reason for the formation of extended planar defects usually associated with higher 3d metals concentration near the film surfaces, interfaces and block boundaries [5, 6].

In ZnO, isovalent substitution of the cation by the 3d metal atom occurs. The low solubility of such atoms (only up to a few tenths of a percent) is an obstacle for creation of the charge carrier concentration necessary for formation of the magnetic ordering caused by the free carriers. On the other hand, strongly nonequilibrium growth of  $\text{Zn}_{1-x}\text{Mn}_x\text{O}$  films leads to the generation of magnetic clusters and secondary structural phases with antiferromagnetic ordering which destroy the magnetic order.

In spite of progress in methods of growing and doping for ZnO films, finding the optimal conditions for the growth of  $\text{Zn}_{1-x}\text{Mn}_x\text{O}$  films with controllable physical properties is still a relevant problem.

The molecular beam epitaxy (MBE) technique makes possible both growth of the most structurally perfect ZnO and  $\text{Zn}_{1-x}\text{Mn}_x\text{O}$  thin films on the (0001)  $\text{Al}_2\text{O}_3$  surface and film doping. However, a large lattice mismatch ( $\sim 30\%$ ) leads to complex transformation of the ZnO film structures, which cannot be observed for the bulk material. This gives new possibilities for functional application of the ZnO/sapphire and  $\text{Zn}_{1-x}\text{Mn}_x\text{O}$ /sapphire systems in optoelectronics.

Structural transformation of ZnO hexagonal cells on the (0001)  $\text{Al}_2\text{O}_3$  interface [7–9] is caused by a large lattice mismatch between film and substrate which may be regarded as the result of relaxation of the strong deformations inherent in such systems. On the other hand, structural transformations are governed by the features of new chemical bonds arising at the ZnO/ $\text{Al}_2\text{O}_3$  interface during film growth and doping. In particular it was shown [7] that, depending on the growth temperature, the hexagonal cells of ZnO film may be rotated in the (0001) plane of the  $\text{Al}_2\text{O}_3$  surface by  $30^\circ$ . Moreover, at elevated growth temperatures, the existence of both types of domains (corresponding to rotated and unrotated ZnO cells) may be observed.

For  $\text{Zn}_{1-x}\text{Mn}_x\text{O}$  films grown on sapphire using pulsed laser deposition (PLD), both rotated and unrotated ZnO domains were observed with x-ray diffraction (XRD) in  $\phi$ -scans [8]. At the same time, for the most structurally perfect specimen with  $x = 0.05$ , only one  $30^\circ$ -rotated domain was seen. Other authors claim [9] that for structurally perfect  $\text{Zn}_{1-x}\text{Mn}_x\text{O}$ /sapphire systems with  $0.01 \leq x \leq 0.25$ , only  $30^\circ$  domains are observed. In addition, the importance of initial growth of buffer ZnO layers and the state of the sapphire the surface for subsequent growth of high-quality ZnO layers have been discussed in a number of papers [10–12].

Therefore, uncertainty about the nature of the rotation of the ZnO hexagonal cell in the (0001)  $\text{Al}_2\text{O}_3$  plane still remains. In particular, rotation it may be induced by stress originating from the lattice mismatch as well as by large concentration of structural defects in the ZnO/sapphire system. In this connection the first-principle methods of interface modeling are important tools to get insight into various interface structures.

In this paper we performed calculations to clarify the nature of the chemical bonds and structural perfection of the ZnO lattice in the vicinity of the interface together with determining of the relative stabilities of various interface structures including rotated and unrotated domains. The important role of zinc and oxygen monolayers on the sapphire surface is predicted using first-principle simulation as well. In addition we investigate structural characteristics of ZnO and  $\text{Zn}_{1-x}\text{Mn}_x\text{O}$  films grown on sapphire using MBE. Employing complex scanning high-resolution optical and x-ray diffraction methods we obtained new information about influence of growth conditions on the physico-chemical properties of ZnO films and their modification after doping with Mn.

## 2. Experimental details

The  $\text{Zn}_{1-x}\text{Mn}_x\text{O}$  films were grown on c-sapphire substrates in a Riber Epineat MBE system with effusion cells designed to be used in ambient oxygen to produce elemental Zn and Mn. Atomic oxygen was supplied via an Addon radiofrequency plasma cell equipped with a high-purity quartz cavity. Prior to the growth, the sapphire substrates were exposed to the oxygen plasma for 20 minutes at  $700^\circ\text{C}$ – $730^\circ\text{C}$  and then cooled down to growth temperature under the plasma-activated O flux. The growth of the  $\text{Zn}_{1-x}\text{Mn}_x\text{O}$  films was carried out at  $560^\circ\text{C}$ , and resulted in 2D growth with facets for the larger Mn contents. The reflection high-energy electron diffraction (RHEED) snapshots can be found in [13]. For comparison, the ZnO reference sample was also grown at  $560^\circ\text{C}$ . While its growth started an 2D, the RHEED patterns turned to 3D during the growth due to a reduction of the Zn sticking coefficient with temperature at  $560^\circ\text{C}$ , the 2D growth regime being maintained only up to  $520^\circ\text{C}$ – $530^\circ\text{C}$  with the Zn/O flux ratio used. The thickness of all films was set at about  $2\mu\text{m}$ .

X-ray investigations were performed using a high-resolution diffractometer PANalytical X'Pert PRO MRD (CuK<sub>α1</sub>-radiation) supplied with a four-bounce asymmetric Ge220 monochromator and a triple-bounce analyzer. The reciprocal space map and diffraction rocking curves obtained in the triple-axis scheme were used to analyze structural parameters. X-ray diffraction patterns and Raman scattering in Zn<sub>1-x</sub>Mn<sub>x</sub>O films were used to ascertain the overall structure and phase purity.

Confocal micro-Raman spectra were collected using a Jobin-Yvon T64000 triple spectrometer equipped with a CCD detector. Measurements were performed using the 488.0 nm line of a mixed Ar<sup>+</sup>/Kr<sup>+</sup> ion laser with output power less than 10 mW. An Olympus BX41 microscope supplied with a ×100 objective possessing NA = 0.90 at room temperature was used to focus laser light on the sample and collect scattered light into the spectrometer. The atomic force microscopy (AFM) measurements were performed by a Dimension 3000 NanoScope IIIa scanning probe microscope. In addition, the Zn<sub>1-x</sub>Mn<sub>x</sub>O samples were studied using the ZEISS EVO-50 scanning electron microscope (SEM).

### 3. Results and discussion

#### 3.1. Surface morphology

Typical SEM images of the surface and cross-section of studied MBE-grown Zn<sub>1-x</sub>Mn<sub>x</sub>O epitaxial films with different Mn concentration are presented in figure 1. The surface morphology of the MBE-grown ZnO epitaxial film was typically quite smooth, consisting of mounds which resulted from kinetic roughening (figure 1(a)). The average mound size is 200 nm, which typically occurs when the growth proceeds by two-dimensional nucleation. The SEM images near the chipped edge of the studied ZnO/sapphire structure show a column-like structure along the growth direction (inset in figure 1). After Mn incorporation, the film surface morphology drastically changes; specifically there is an increase in the irregularity of the film (figures 1(b), (c)). This caused reduction of the average mound size from 130 to 80 nm with increasing Mn concentration in the Zn<sub>1-x</sub>Mn<sub>x</sub>O films from x = 2% to 7%, respectively.

The average surface roughness  $R_a$  of Zn<sub>1-x</sub>Mn<sub>x</sub>O films, determined using AFM, increases with increasing of Mn concentration in Zn<sub>1-x</sub>Mn<sub>x</sub>O with x = 0% (1.8), 2% (3.5) and 7% (5.0), respectively. Such behaviour is consistent with previous studies [14] where increased dislocation density in nitride films with decreasing surface roughness was observed (see table 1).

#### 3.2. Structural analysis

X-ray diffraction measurements were performed to investigate the crystal structure of Zn<sub>1-x</sub>Mn<sub>x</sub>O films grown on an Al<sub>2</sub>O<sub>3</sub> substrate (figure 2). Symmetrical (0002) and (0004) reflections from Zn<sub>1-x</sub>Mn<sub>x</sub>O films in 2θ XRD spectra are indicative of their mono-phase wurtzite structure (P6<sub>3</sub>mc space group). The (0006) reflection in the XRD spectra corresponds to an Al<sub>2</sub>O<sub>3</sub> substrate, while the high intensity of the (0002) reflection affirms that epitaxial Zn<sub>1-x</sub>Mn<sub>x</sub>O film was grown in the [001] crystallographic direction (on a c-sapphire face). This correlates with SEM measurements of such films (figure 1).

The lattice parameters of undoped ZnO film (a = 3.2495 Å, c = 5.2069 Å) correlate well with the parameters of bulk crystal (a = 3.2495–3.2501 Å, c = 5.2057–5.206 Å) [15], that confirms the high quality of the wurtzite crystal structure of undoped ZnO film. As can be seen from the inset in figure 2, increasing the Mn concentration in Zn<sub>1-x</sub>Mn<sub>x</sub>O film leads to an increase of the lattice parameter c as a result of the substitution of the Mn<sup>2+</sup> (0.66 Å) ions for Zn<sup>2+</sup> (0.60 Å). For the Zn<sub>1-x</sub>Mn<sub>x</sub>O films under investigation, the positions of recorded (0002) reflexes are shifted as compared with the corresponding values for ZnO single-crystal (34.40°) when the concentration of Mn atoms is increased.

The XRD spectra in figure 2 show a decrease in peak intensity and an increase in the full width at half maximum (FWHM) for the (002) reflections with the increase of Zn<sub>1-x</sub>Mn<sub>x</sub>O film doping owing to the presence of residual micro stress in the films. For Mn-doped ZnO films, secondary structural phases such as MnO, MnO<sub>2</sub>, Mn<sub>3</sub>O<sub>4</sub> and Zn<sub>3</sub>Mn<sub>3-x</sub>O<sub>4</sub> were not registered in 2θ XRD spectra reflexes. This confirms the uniform embedding of Mn atoms in ZnO wurtzite lattice.

It is known that stress in the Zn<sub>1-x</sub>Mn<sub>x</sub>O films is a result of both intrinsic and extrinsic components [16, 17]. The intrinsic component is related to the trapped point defects (interstitial Zn atoms and oxygen vacancies) and to extended defects (dislocations, stacking faults and twins) that appear as a result of deviation from the equilibrium growth conditions and Mn doping. The macro stress arising is related to the lattice parameters ( $\sigma_{\text{lat}}$ ) and thermal expansion coefficients ( $\sigma_{\text{th}}$ ) mismatch between Zn<sub>1-x</sub>Mn<sub>x</sub>O film and Al<sub>2</sub>O<sub>3</sub> substrate, and is defined as  $\sigma_{\text{xx}} = \sigma_{\text{th}} + \sigma_{\text{lat}}$ .

The magnitude of residual deformation in Zn<sub>1-x</sub>Mn<sub>x</sub>O film on an Al<sub>2</sub>O<sub>3</sub> substrate is mainly defined by  $\epsilon_{\parallel}^{\text{lat}}$  (deformation caused by a mismatch in the lattice parameters between the film and substrate) as well as by the thermal deformation  $\epsilon_{\parallel}^{\text{therm}}$ , which is one order of magnitude smaller. The lattice parameter mismatch between,

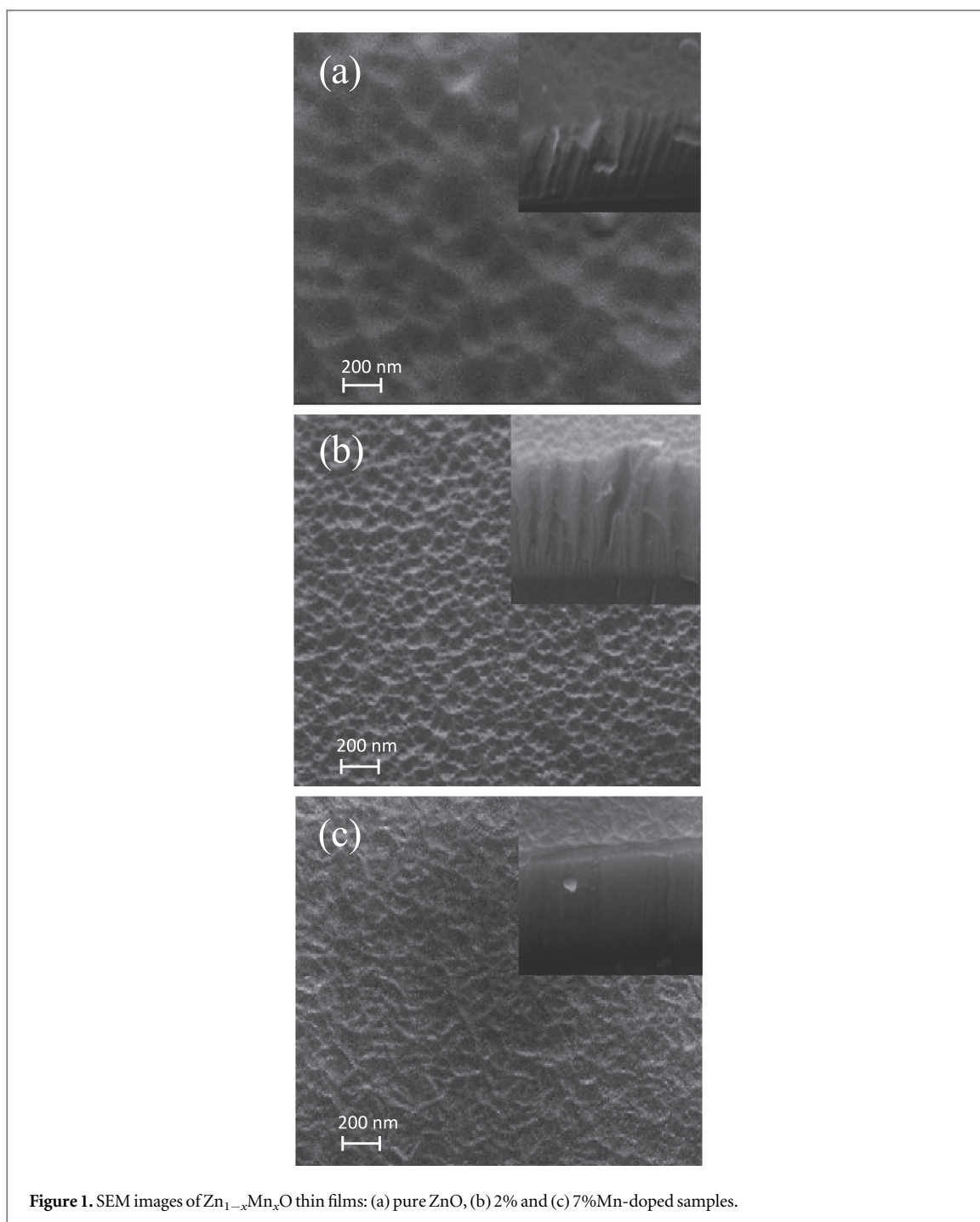


**Figure 1.** SEM images of  $Zn_{1-x}Mn_xO$  thin films: (a) pure ZnO, (b) 2% and (c) 7% Mn-doped samples.

**Table 1.** The properties of  $Zn_{1-x}Mn_xO$  films. The  $\epsilon_{xx}$  and  $\epsilon_{zz}$  strain components, LCL and screw dislocation density ( $N_s$ ) are given.

$x$	$\epsilon_{xx}$	$\epsilon_{zz}$	$a$ (nm)	$c$ (nm)	LCL (nm)	$N_s$ $10^{10}(\text{cm}^{-1})$
0	0.00127	-0.00075	0.3254	0.5203	889	6.95
0.02	0.00156	-0.0016	0.3258	0.52045	738	7.18
0.07	0.00186	-0.0020	0.3264	0.52076	413	9.72

the undoped ZnO ( $a_{\text{ZnO}} = 3.25 \text{ \AA}$ ) and  $\text{Al}_2\text{O}_3$  ( $a_{\text{Al}_2\text{O}_3} = 4.75 \text{ \AA}$ ) is defined as  $f_{\text{mis}} = (a_{\text{ZnO}} - a_{\text{Al}_2\text{O}_3}) / a_{\text{Al}_2\text{O}_3} \times 100\%$ , and is on the order of  $-30\%$ . In this case the negative sign indicates the tensile deformation on the ZnO/ $\text{Al}_2\text{O}_3$  interface [18]. Figure 3 displays the in-plane azimuthal angle scans of the  $Zn_{1-x}Mn_xO$  films. The scanning planes used here were (10 – 11) for ZnO and (11 – 21) for sapphire. It is seen that the wurtzite (10 – 11) in-plane direction is parallel to the (10 – 12) plane of sapphire, indicating a  $30^\circ$  rotation of the ZnO

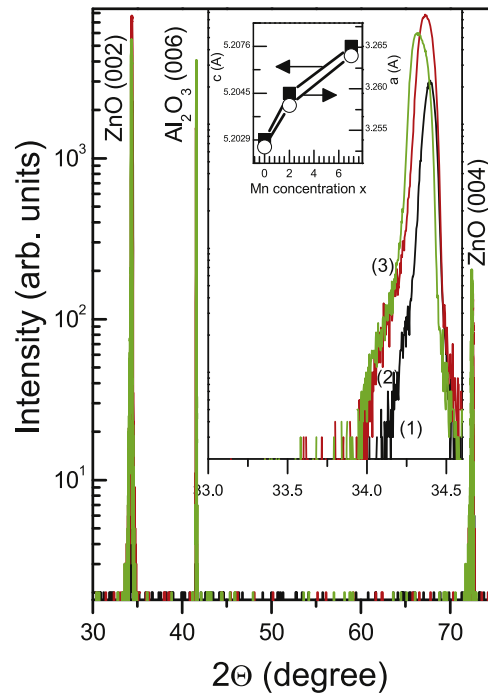


**Figure 2.**  $2\theta$  XRD spectra of the  $Zn_{1-x}Mn_xO$  films: (1) pure ZnO, (2) 2%, (3) 7% Mn-doped samples. The dependence of the lattice parameter  $c$  for  $Zn_{1-x}Mn_xO$  films on the Mn concentration is shown in the inset. The error bars shown therein are determined by the errors in XRD peak positions.

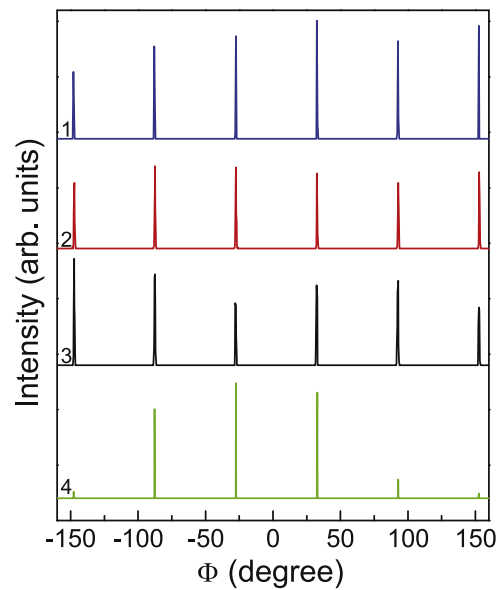


**Figure 3.** The  $\Phi$ -scan of  $Zn_{1-x}Mn_xO$  thin films: (1) pure ZnO, (2) 2%, (3) 7% Mn-doped samples in the (10–11) plane and (4)  $Al_2O_3$  substrate in the (11 – 21) plane.

unit cell with respect to that of the  $Al_2O_3$  substrate. In this case the lattice parameter mismatch between ZnO ( $a_{ZnO} = 3.25 \text{ \AA}$ ) and  $Al_2O_3$  ( $a_{Al_2O_3} = 2.75 \text{ \AA}$ ) is +18% [19]. The rotation of ZnO mosaic blocks on the  $Al_2O_3$  substrate leads to compressive deformation of the ZnO films. The increase in the Mn concentration causes the same rotation angle,  $30^\circ$ , for both  $x = 2\%$  and  $7\%$ .

The in-plane ( $\epsilon_{xx} = \epsilon_{yy}$ ) and out-of-plane ( $\epsilon_{zz}$ ) strain components of  $Zn_{1-x}Mn_xO$  films were calculated according to equations (1), (2), and (3) [20, 21] and equation (4) [22]:

$$\epsilon_{xx} = \epsilon_{yy} = \frac{a - a_0}{a_0}, \quad (1)$$

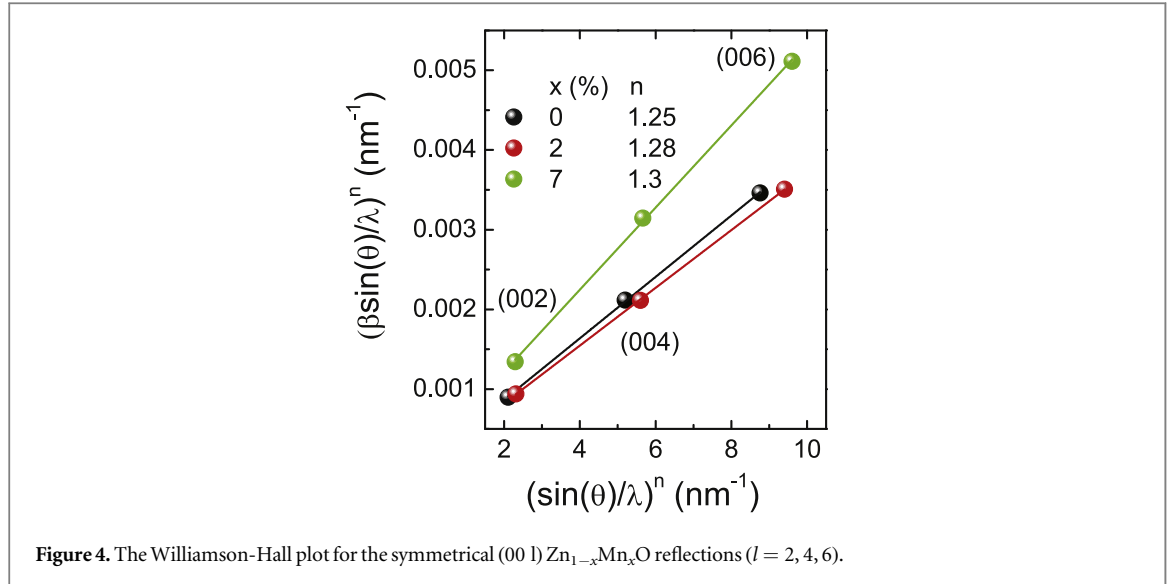


Figure 4. The Williamson-Hall plot for the symmetrical (00 l)  $Zn_{1-x}Mn_xO$  reflections ( $l = 2, 4, 6$ ).

$$\epsilon_{zz} = -\frac{C_{13}}{C_{33}}(\epsilon_{xx} - \epsilon_{yy}), \quad (2)$$

$$\epsilon_{zz} = \frac{c - c_0}{c_0}, \quad (3)$$

$$A^{Zn_{1-x}Mn_xO} = xA^{MnO} + (1 - x)A^{ZnO}, \quad (4)$$

where  $a$  and  $c$  are measured lattice parameters.  $A$  in equation (4) stands for lattice parameters and elastic stiffness coefficients ( $a_0$ ,  $c_0$ ,  $C_{13}$  and  $C_{33}$ , respectively) which correspond to the fully relaxed  $Zn_{1-x}Mn_xO$  film.  $A^{MnO}$  and  $A^{ZnO}$  refer to the values for the bulk crystals [23, 24].

From the inset in figure 2 it is clear that  $Zn_{1-x}Mn_xO$  films undergo tensile strain in the  $x$  and  $y$  directions, and that the magnitude of the strain increases with Mn concentration [19]. The deformation value  $\epsilon_{\parallel}^{lat}$  for undoped ZnO film is  $1.27 \cdot 10^{-3}$  and corresponds to tensile deformation in the ZnO growth plane. As can be seen from table 1, the increase in the Mn concentration in  $Zn_{1-x}Mn_xO$  films leads to an increase in the  $\epsilon_{\parallel}^{lat}$  deformation from  $1.56 \cdot 10^{-3}$  to  $1.86 \cdot 10^{-3}$  for  $x = 2\%$  and  $7\%$ , respectively.

Since the  $Zn_{1-x}Mn_xO$  film thickness exceeds the critical value, and the film is partially relaxed due to the dislocation density on the order of  $10^{11} \text{ cm}^{-2}$ , we conclude that the residual deformation in the  $Zn_{1-x}Mn_xO$  films is caused by the mismatch of the thermal expansion coefficients ( $a_{\parallel}^{Al_2O_3} = 5.25 \cdot 10^{-6} \text{ K}^{-1}$  for  $Al_2O_3$ [25], and  $a_{\parallel}^{ZnO} = 4.75 \cdot 10^{-6} \text{ K}^{-1}$  for ZnO [26]). Since  $a_{\parallel}^{Al_2O_3} > a_{\parallel}^{ZnO}$  at room temperature, a tensile deformation in the growth plane of ZnO occurs, which correlates with the experimental data.

The Williamson-Hall procedure for the x-ray diffraction peak (XDP) broadening analysis was applied for symmetrical (002), (004) and (006) $\omega$ -scans (figure 4). We have used the Pseudo-Voigt function to fit the XDPs. The lateral correlation length (LCL) and tilt ( $\alpha$ ) distribution of the mosaic blocks are the main reasons for the broadening of the XDPs and can be separated by plotting  $(\beta \sin(\theta)/\lambda)^n$  against  $(\sin(\theta)/\lambda)^n$  for each reflection and can be fitted with a straight line [27, 28]. Here,  $\beta$  is the FWHM of the XDP,  $2\theta$  is the scattering angle,  $\lambda$  is the x-ray wave length and  $n$  takes values from 1 to 2 ( $n = 1 + (1 - f)^2$ ) depending on the value of  $f$  which define the Lorentzian content in the Pseudo-Voigt distribution.

The Williamson-Hall plots for  $Zn_{1-x}Mn_xO$  films are shown in figure 4. From the intersection of the fitted line with the ordinate axis ( $y_0$ ) the LCL can be estimated ( $LCL = 0.9/2y_0$ ), whereas the average value of  $\alpha$  is obtained from the slope of the linear dependence. The LCL values of investigated  $Zn_{1-x}Mn_xO$  films are listed in table 1. The average values of  $LCL = 889 \text{ nm}$  and  $\alpha = 0.047^\circ$  for undoped ZnO film were obtained and can be compared to the average size of columns. Besides, as can be seen from table 1, the LCL decrease with the increase in Mn doping. Since the increase in doping of  $Zn_{1-x}Mn_xO$  films leads to an increased density of crystallization centers (nucleation), this results in a decrease in the of average column size in doped films.

### 3.3. Raman scattering

ZnO crystallizes in the hexagonal wurtzite structure and belongs to the  $P6_3mc$  space group with four atoms per primitive unit cell. According to the group theory analysis in the  $\Gamma$ -point of the ZnO Brillouin zone, phonon modes belong to the following irreducible representations:  $\Gamma_{opt} = A_1(Z) + 2B_1 + E_1(X, Y) + 2E_2$ , where  $X$ ,  $Y$  and  $Z$  are directions of light polarization. Modes with  $A_1(Z)$ ,  $E_1(X, Y)$  and  $E_2$  symmetries are active in Raman

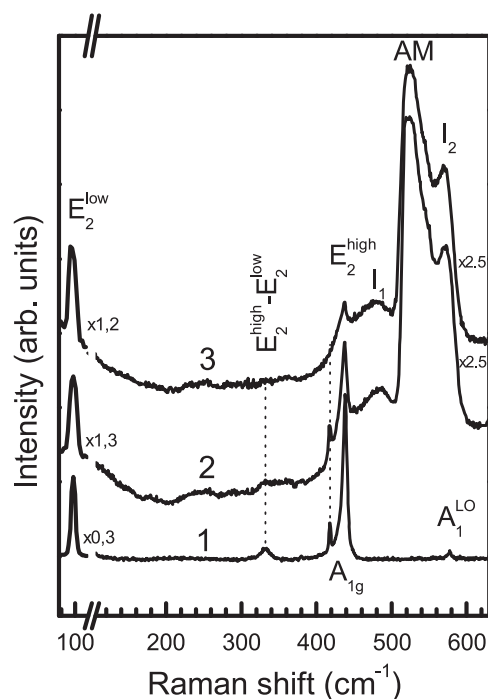


Figure 5. Raman spectra of  $Zn_{1-x}Mn_xO$  thin films: (1) pure ZnO, (2) 2% and (3) 7% Mn-doped samples.

spectra, while the modes with  $B_1$  symmetry are the so-called ‘silent’-modes i.e., these modes cannot be observed in Raman spectra. Phonon modes of  $A_1$  and  $E_1$  symmetries correspond to vibrations of atoms along and perpendicular to the crystallographic  $c$ -axis, respectively. These polar modes are split in  $\Gamma$ -point on the longitudinal (LO) and transverse (TO) optical phonon branches by the longitudinal macroscopic electric field. The non-polar  $E_2^{\text{high}}$  phonon mode corresponds to vibrations of oxygen atoms in the anion sublattice, while  $E_2^{\text{low}}$  corresponds to vibrations of atoms in the cation (Zn) sublattice in the plane perpendicular to the  $c$ -axis of wurtzite ZnO. All micro-Raman spectra were registered in  $z(x, x)\bar{z}$  backscattering geometry ( $z$ -direction is parallel to the wurtzite  $c$ -axis). It should be noted that in the first order Raman spectra of the  $Zn_{1-x}Mn_xO$  films scattering on  $A_1(\text{LO})$ ,  $E_2^{\text{low}}$  and  $E_2^{\text{high}}$  phonon modes is allowed.

Figure 5 shows the Raman spectra of undoped ZnO film grown on a (0001)- sapphire substrate. The appearance in Raman spectra of intense  $E_2^{\text{low}}$  and  $E_2^{\text{high}}$  phonon modes at 99.3 and 438.3  $\text{cm}^{-1}$  with FWHM ( $\Gamma$ ) equal to  $\sim 1.6$  and 5.9  $\text{cm}^{-1}$ , respectively, confirms the high quality wurtzite structure of the undoped ZnO films [29, 30].

The frequency position of the  $E_2^{\text{high}}$  phonon mode of ZnO films is shifted to the high-frequency side by  $\Delta\omega \approx 1.3 \text{ cm}^{-1}$  compared with the corresponding frequency for bulk ZnO (437.0  $\text{cm}^{-1}$ ). This is a consequence of the presence of tensile strain in the plane perpendicular to the  $c$ -axis and rotation of the ZnO unit cell by  $30^\circ$  relative to the sapphire substrate, which is consistent with XRD data (table 1). The phonon mode at 332.0  $\text{cm}^{-1}$  corresponds to the two-phonon  $E_2^{\text{high}} - E_2^{\text{low}}$  scattering which follows from the temperature dependence of the scattering intensity. In Raman spectra the low-intensity phonon line at 574.0  $\text{cm}^{-1}$  is characteristic of the high-crystal quality of ZnO films due to the process of destructive interference between the Florich mechanism of interaction and the deformation potential in the LO phonon scattering process in ZnO [31]. Also, in the Raman spectra of the investigated films, the phonon mode of  $A_{1g}$  symmetry at 418  $\text{cm}^{-1}$  originating from the sapphire substrate is recorded.

After the incorporation of Mn into the films a low-frequency shift, a reduction of the intensity, and as well as an increase of the FWHM were observed for the  $E_2^{\text{high}}$  and  $E_2^{\text{low}}$  phonon modes, as compared with pure ZnO film (figure 5). This is caused by an increase of the structural disorder in  $Zn_{1-x}Mn_xO$  films. Moreover, we note that phonon bands that correspond to formation of secondary structural phases or precipitates, such as  $MnO$ ,  $MnO_2$ ,  $ZnMn_3O_4$  or  $Zn_xMn_{3-x}O_4$  [32], were not registered in the Raman spectra of the investigated  $Zn_{1-x}Mn_xO$  films. This suggests that Mn atoms can be incorporated into the wurtzite ZnO structure as substitutional or interstitial defects, or are localized at the complicated interfaces and boundaries.

In the Raman spectra of  $Zn_{1-x}Mn_xO$  films, the so-called additional mode (AM) at  $\sim 520 \text{ cm}^{-1}$  is recorded [33, 34]. The appearance of this band may be considered as confirmation of the embedded atom model. In this

**Table 2.** Frequency position  $\omega_0$ , FWHM  $\Gamma$ , value the asymmetrical ratio  $\Gamma_{\text{left}}/\Gamma_{\text{right}}$  and correlation length  $L$  of phonon modes of  $\text{Zn}_{1-x}\text{Mn}_x\text{O}$  films.

$x$	$\Gamma$ ( $\text{cm}^{-1}$ )	$\Gamma_{\text{left}}/\Gamma_{\text{right}}$	$\omega_0$	$L$ (nm)
0	5.87	1.32	438.34	$36.8 \pm 2.0$
0.02	8.62	1.23	437.74	$16.7 \pm 1.0$
0.07	14.18	1.12	437.03	$10.8 \pm 1.0$

case AM mode is treated as local vibrations of Mn atoms incorporated in cation sublattice of ZnO (figure 5). The intensity, frequency and form of the AM mode do not depends on the concentration of Mn at  $x < 0.1$ , confirming the assumption of the formation of a  $\text{Zn}_{1-x}\text{Mn}_x\text{O}$  film. This band lies in the  $500\text{--}600\text{ cm}^{-1}$  spectral region and has an asymmetrical and broad shape. At least two Lorentzian contours are necessary to provide the best fit to its shape.

Polarization measurements in backscattering geometry, namely  $x(z, z)\bar{x}$ ,  $z(x, x)\bar{z}$  and  $x(y, y)\bar{x}$  did not register any changes of AM in Raman spectra of  $\text{Zn}_{1-x}\text{Mn}_x\text{O}$  films. This means that AM mode is not responsible for the phonons with  $A_1$  and  $E_2$  symmetries permitted in these scattering geometries. Also, the shape of the AM recorded at low temperature (6 K) depends on the excitation energy and has the opposite temperature dependence to that of the phonon bands. These facts indicate the electron-phonon nature of AM and  $I_2$  bands.

In the Raman spectra of doped  $\text{Zn}_{1-x}\text{Mn}_x\text{O}$  films the  $I_1$  broad band in the frequency range of  $445\text{--}500\text{ cm}^{-1}$  is registered (figure 5). To elucidate the nature of this band we note that electron microscopic studies have proved that the morphology of the surface was changed after Mn doping. In particular, the average mound size is decreased while roughness is increased. As a consequence, the relative number of atoms located near the surface and interface is increased as compared with the ones in the interior of the of film. This can lead to registration of the surface optical mode (SOP) in the Raman spectra of ZnO films [35], nanorods [36] and nanoparticles [37] doped with transition metal atoms. Since the  $I_1$  band is detected in the frequency range between the LO and TO phonon modes and its frequency position does not change with increasing Mn concentration,  $I_1$  can be attributed to the surface vibrations in  $\text{Zn}_{1-x}\text{Mn}_x\text{O}$  films.

Figure 5 shows that when the Mn concentration in  $\text{Zn}_{1-x}\text{Mn}_x\text{O}$  films is increased, an increase in the FWHM for the  $E_2^{\text{high}}$  phonon mode is observed. Also, the low-frequency asymmetry broadening occurs compared with undoped ZnO film due to the effect of spatial localization of phonons. A model of strong spatial localization of phonons (spatial correlation model SCM) was first developed by Richter for nc-Si of spherical form [38] and later extended by Campbell [39] to different shapes of nanocrystallites. It can manifest itself as a shift and asymmetrical broadening of the fundamental phonon modes depending on the size and form of nano-objects.

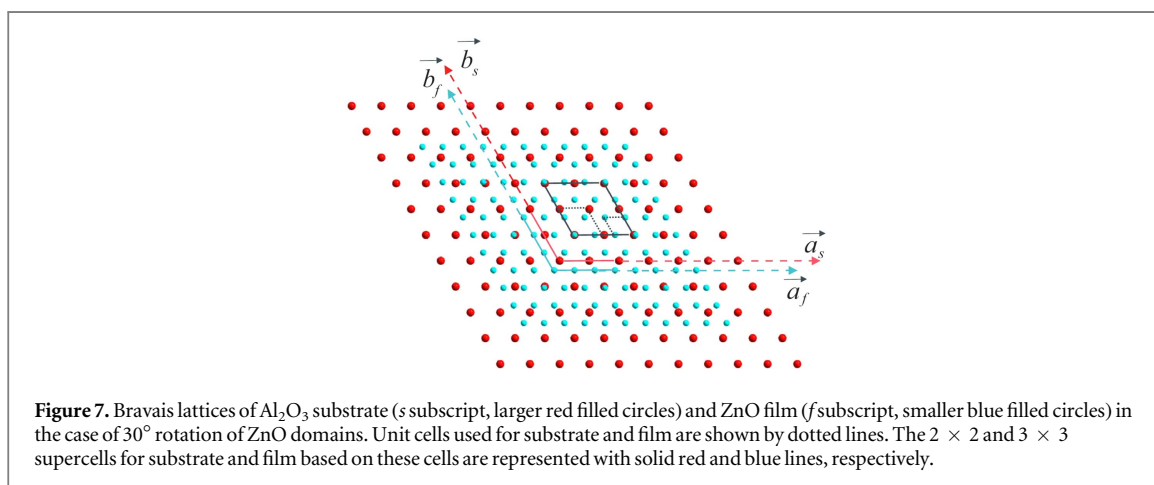
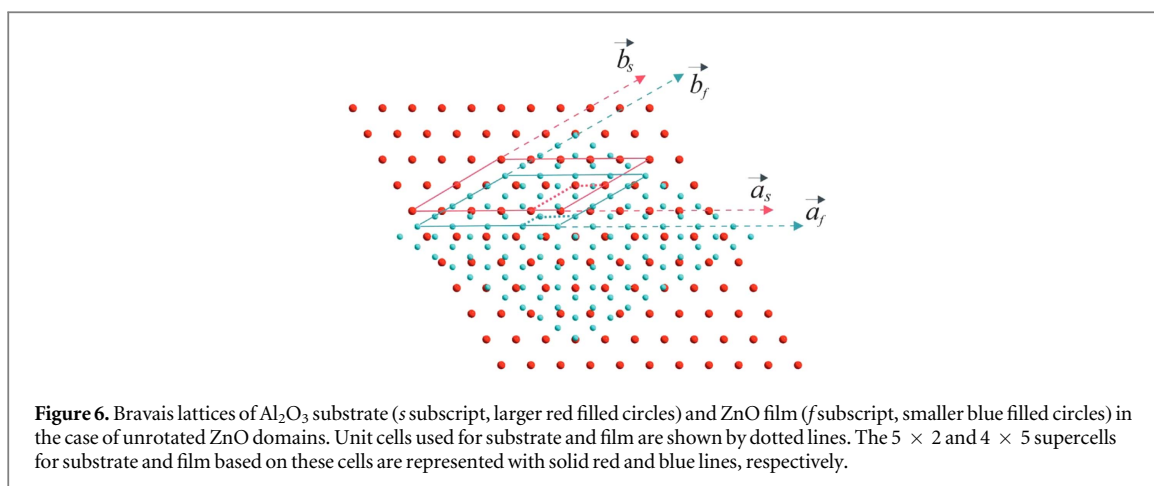
The phonons with wave vectors  $q = 0$  (the center of the Brillouin zone) can only take part in the Raman scattering process in the ZnO bulk crystals for symmetrical lines with Lorentz shape. In Mn-doped ZnO films the infinite lattice periodicity is violated, i.e. phonons are spatially limited by the small size of the periodic structure. This leads to an uncertainty in the value of the wave vector  $\vec{q} \neq 0$ , and phonons from all points of the Brillouin zone can appear in the Raman spectra.

Due to the downward behaviour of dispersion  $E_2^{\text{high}}$  phonon branches in the vicinity of the  $\Gamma$  point, the low-frequency shift and asymmetric broadening of the  $E_2^{\text{high}}$  phonon modes are observed in Raman spectra of the  $\text{Zn}_{1-x}\text{Mn}_x\text{O}$  films as compared with the corresponding spectra of the undoped ZnO film. The SCM model allows characterization of crystal lattice quality by introducing an important parameter  $L$  - 'correlation length.' The low-frequency phonon mode shift is proportional to correlation length, which is the average size of the material homogeneity, i.e. the average distance between defects (e.g., twins, stacking faults, vacancies, boundaries, pores etc [40]). According to theoretical models of spatial localization (confinement) developed by Richter [38, 39] the intensity of phonon  $I(\omega)$  mode can be written as

$$I(\omega) = \int_{\vec{q}} \frac{|C(0, q)|^2 d^3q}{(\omega - \omega(q))^2 + (\Gamma_0/2)^2}, \quad (5)$$

where  $|C(0, q)|^2 = \exp[-(q^2L^2/4)]$  is the Fourier coefficient,  $\Gamma_0 = 6\text{ cm}^{-1}$  is the FWHM for the phonon mode of undoped ZnO film,  $\omega(q)$  is the dispersion of the  $E_2^{\text{high}}$  phonon branch vibrations, which can be represented as  $\omega(\kappa) = A + B \cos(\pi\kappa)$  with  $A = \omega_0$  (see table 2) and  $B = 12.5\text{ cm}^{-1}$  for the  $E_2^{\text{high}}$  phonon mode of bulk ZnO [41]. The integration in equation (5) is carried out over the entire Brillouin zone.

Simulations of experimental Raman spectra of  $\text{Zn}_{1-x}\text{Mn}_x\text{O}$  films according to equation (5) have allowed determination of a phonon correlation length (PCL) (see table 2). We note that LCL measured by XRD provides an estimate of the size of nearly perfect crystal domains over which the crystalline order exists. This coherence length is sensitive to imperfections comparable to the x-ray wavelength (0.154 nm), and thus reflects the presence of crystallographic disorder and extended defects. In contrast the PCL allows one to obtain a



quantitative estimate of volumes with perfect structure and is sensitive, among other things, to alloy fluctuations (i.e. to a nonuniform distribution of Mn) in the single crystalline column of  $\text{Zn}_{1-x}\text{Mn}_x\text{O}$  films. The existence of such fluctuations in doped films decreases the finite phonon propagation from  $L = 37$  nm to 10 nm for a variation of Mn concentration from  $x = 0$  to 7%. For the undoped ZnO film, the obtained PCL value of 37 nm agrees well with data presented in [19]. Namely it was shown that 2D ZnO layers grown by MBE on sapphire consist of a mosaic structure with columnar subgrains with diameters ranging from 25 to 75 nm. In contrast the LCL value corresponds to a relatively large film area which includes adjacent crystallites with nearly equal tilt and twist angles. This parameter depends indirectly on the Mn content through influence of the doping on the film morphology, 2D versus 3D growth mode, dislocation density and nonuniformity of Mn distribution (see figure 1 and table 1).

#### 4. First-principle modelling of the $\text{Al}_2\text{O}_3/\text{ZnO}$ interface

It is well known that in the case of a small lattice mismatch ( $\sim 1\%$ ) between the substrate and deposited film, *ab initio* simulation of the interface is a relatively simple task and most current investigations avoid going beyond these limits [42]. In our case of ZnO films deposited on the bulk sapphire substrate the mismatch between primitive lattice cells is as large as 30% and the cannot be fitted to one another. A possible solution to this problem is accommodation of supercells instead of  $(1 \times 1)$  conventional cells [43]. In particular, if an  $(m \times n)$  supercell for the substrate coincide well with a  $(k \times l)$  supercell for the deposited film then it may be used for the first-principle interface modelling.

In the case of ZnO film on an  $\text{Al}_2\text{O}_3$  substrate two possibilities must be considered. The first corresponds to the case where the axes of conventional cells for both film and substrate are parallel, while the second possibility corresponds to rotation of the film by  $30^\circ$  with respect to the substrate. In accordance with experiment [7, 25, 44] both possibilities of film growth may be realized depending on the growth conditions. To simulate the structure and energetics of such interfaces one must choose the appropriate supercells, as shown in figure 6 and 7 for unrotated and rotated films, respectively. In particular the  $(2 \times 2)$  conventional hexagonal cell for the  $\text{Al}_2\text{O}_3$

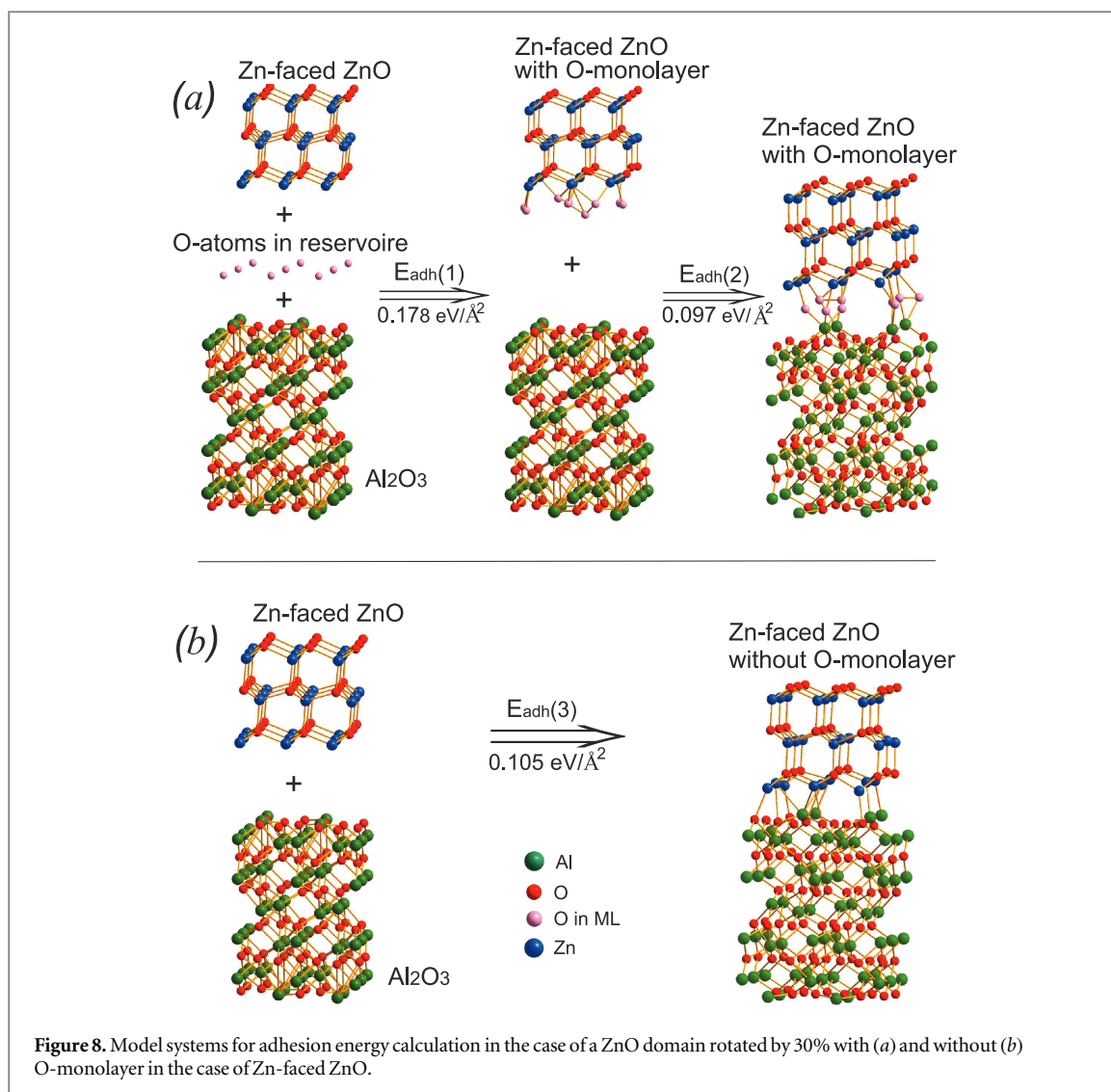


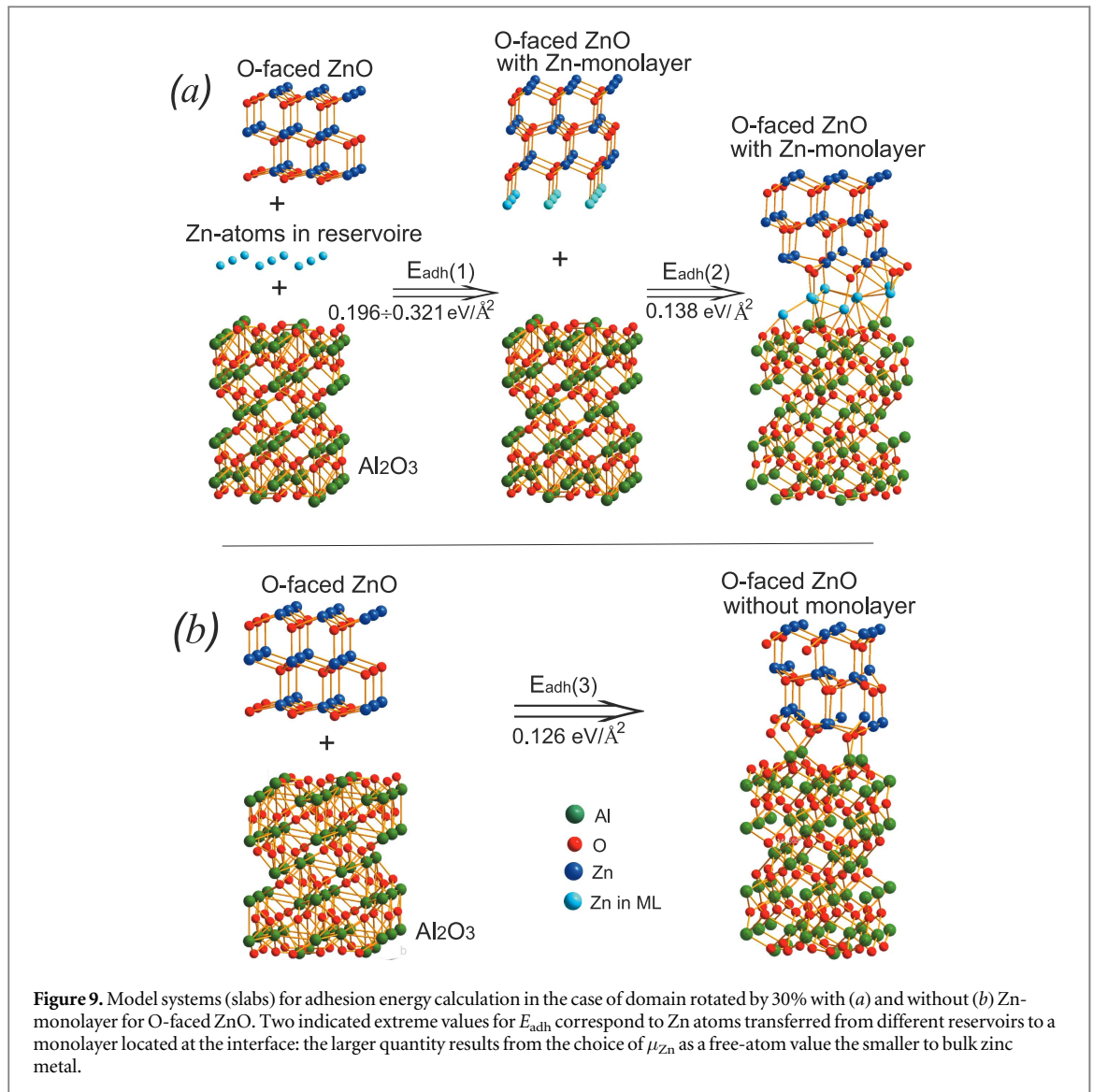
**Table 3.** Calculated energy gain when Zn or O monolayers are introduced at the ZnO/Al<sub>2</sub>O<sub>3</sub> interface. The number of atoms in the monolayer is equal to 20 in the case of unrotated ZnO film and 9 in the case of a rotated film. The upper limit for  $\Delta E$  for a Zn-monolayer corresponds to the free atom and lower limit corresponds to the chemical potential of Zn atoms in a bulk metal.

Atoms of monolayer	Termination of ZnO surface	ZnO slab	$\Delta E$ (eV/Å <sup>2</sup> )
O	Zn	Rotated	0.171
Zn	O	Rotated	0.208–0.333
O	Zn	Unrotated	0.131
Zn	O	Unrotated	0.170–0.280

substrate in figure 7 fits the (3 × 3) cell of rotated ZnO films well (the mismatch is only 2.3%, which induces compressive strain in ZnO films).

For unrotated films we use the supercells based on the nonconventional cells for both sapphire and ZnO as shown in figure 7. In this case the (5 × 2) supercell for Al<sub>2</sub>O<sub>3</sub> coincides with the (4 × 5) one for ZnO with a relatively small mismatch of 1.5% in the *b* direction and 5.7% in the *a* direction, leading to stretch deformation of grown ZnO film. However, the computational demands of this approach become heavy and so it has seldom been used in practice.

For this reason we perform first-principle DFT calculations using Siesta [45, 46], which at present is one of the fastest DFT codes due to its use of a numerical basis that has possess the value of exactly zero beyond the cut-off radius. Modelling of the interface was carried out using periodic slab calculations with a cell size equal to



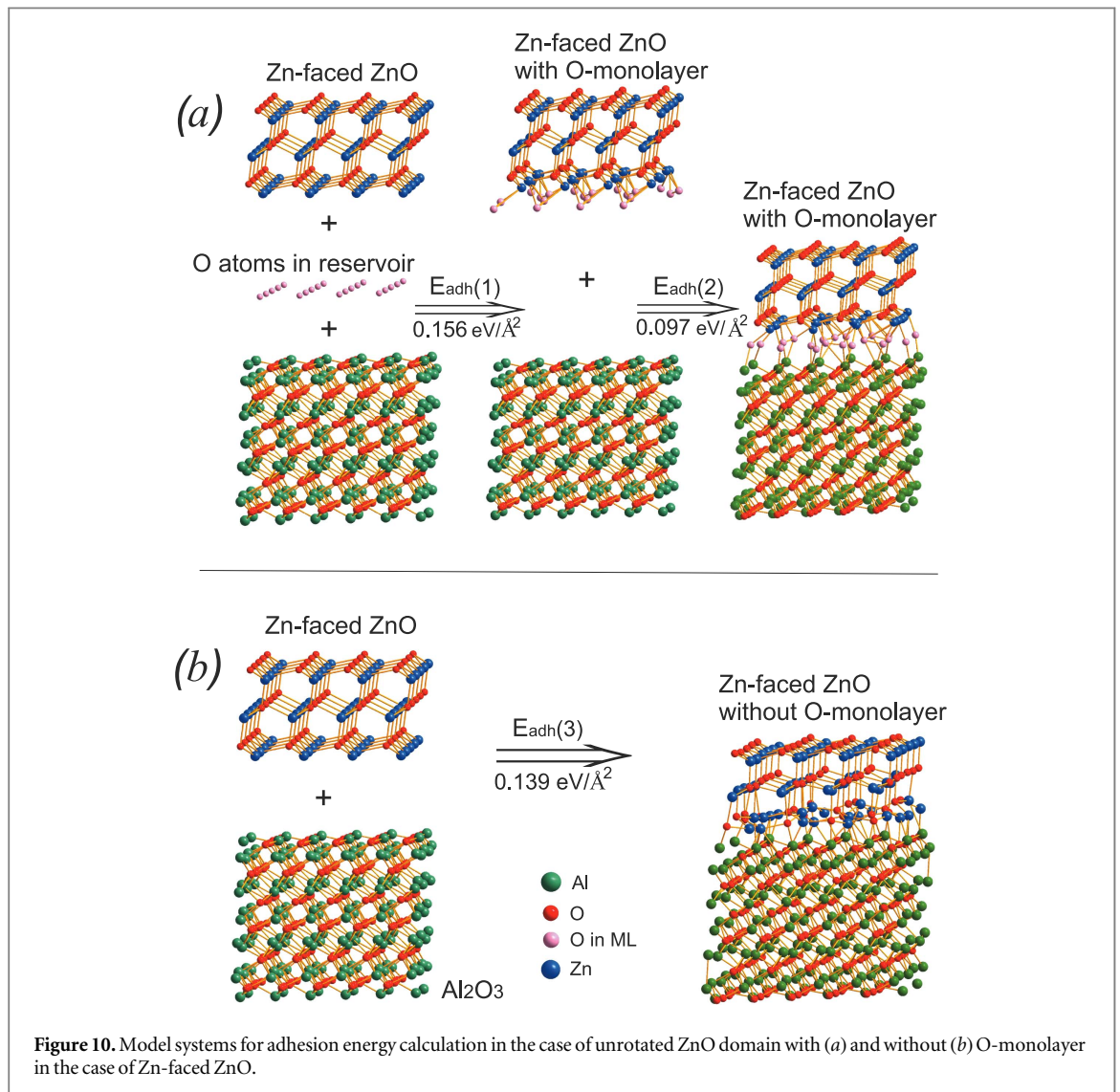
40 Å in the  $z$  direction in all cases. This ensures a minimum of 20 Å of empty space between slabs which were used for simulation of various types of interfaces and their constituents.

The GGA exchange-correlation functional of Perdew, Burke and Ernzerhof (PBE) [47, 48], the  $(2 \times 2 \times 1)$  Monkhorst-Pack grid for integration over the Brillouin zone, and a double-zeta plus polarization basis for atoms of Zn, O and Al (DZP) were used. Herein semicore 3d electrons for Zn atoms were treated as the valence ones. Back surfaces of ZnO-related slabs were saturated with pseudohydrogens ( $Z = 0.5$  or  $Z = 1.5$ ) supplied with a single-zeta basis to enhance the self-consistent field convergence and save computation time. In all cases norm-conserving pseudopotentials of Troullier-Martins type [49] were employed. In addition, Fermi level smearing [50] with electronic temperature of 0.01 Ry was used to eliminate the SCF convergence problems. The influence of this parameter on the calculated energy differences normalized on the surface area is negligibly small.

For simulation of the ZnO/sapphire interface we suppose that the lattice constant of thin ZnO film always accommodates to the one for bulk sapphire. For slabs containing both ZnO and Al<sub>2</sub>O<sub>3</sub> (or only Al<sub>2</sub>O<sub>3</sub>) we used the experimental bulk lattice constant for Al<sub>2</sub>O<sub>3</sub>, while for a ZnO slab alone we use the experimental value for bulk a ZnO. The sizes of sapphire slabs in the  $z$  direction correspond to the size of conventional cells for bulk crystal (12.991 Å). The wurtzite ZnO slabs used for calculations contain three double ZnO layers with capped bond pseudohydrogens on the back surface of a slab. The geometry optimization in all cases was performed without any constraints. In this a way, the initial stage of ZnO film growth is simulated.

#### 4.1. Structure of Al<sub>2</sub>O<sub>3</sub> surface: comparison with other calculations and experiment

It is generally accepted [51] that the most stable surface termination of  $\alpha$ -Al<sub>2</sub>O<sub>3</sub> (0001) is a single Al layer. Hereat, the first Al–O interlayer spacing is significantly contracted (down to 0.4 Å) as compared with the bulk



spacing equal to 0.83 Å. Qualitatively, this means that oxygen atoms shift up and are placed close to the surface. Early first principle LDA-based calculations [52] qualitatively confirm this experimental conclusion. However, the calculated Al–O interlayer spacing is underestimated and as only 0.128 Å. Our calculations using GGA PBE functional give a somewhat better value of 0.224 Å. We notice that in this case comparison of calculated values with experimental result is not straightforward because of strong anharmonicity suggested for atoms located on the Al<sub>2</sub>O<sub>3</sub> surface [49].

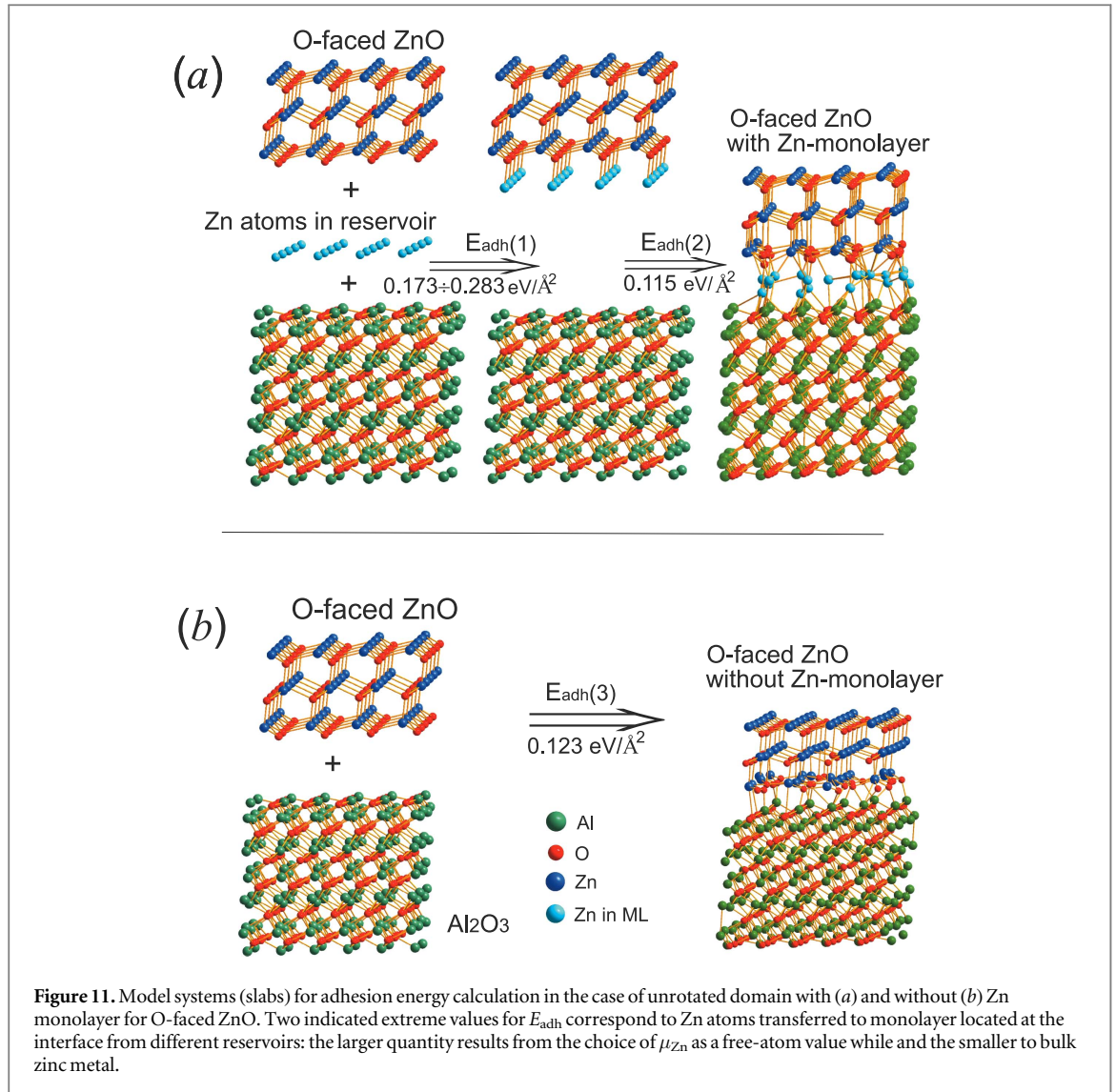
One may suppose that this surface structure when both Al and O atoms of the first and second layers are located near the sapphire surface facilitates creation of additional bonds and increases the adhesion energy of the ZnO film to the sapphire substrate.

#### 4.2. Zinc and oxygen monolayers located at the interface—new insight into the interface structure

A priori one can suppose that there is a conventional structure of interface between ZnO and Al<sub>2</sub>O<sub>3</sub> as shown in figures 8(b)–11(b). The adhesion energy may be defined as the energy difference between slabs representing isolated ZnO and Al<sub>2</sub>O<sub>3</sub> and a structure with the corresponding interface:

$$E_{\text{adh}} = E_{(\text{ZnO})} + E_{(\text{Al}_2\text{O}_3)} - E_{(\text{ZnO} + \text{Al}_2\text{O}_3)}, \quad (6)$$

It is seen that the adhesion energy is sufficiently large to form the stable interface in the cases of both O-faced and Zn-faced ZnO surfaces. However one may predict the existence of different interface structures which are energetically preferable. We suppose that the interface is in thermodynamic equilibrium with reservoirs containing Zn and O atoms with chemical potentials  $\mu_{\text{Zn}}$  and  $\mu_{\text{O}}$ , respectively. Then we insert an additional monolayer of O (Zn) atoms between the Zn-faced (O-faced) surface of ZnO and the Al<sub>2</sub>O<sub>3</sub> and calculate an energy gain according to relations these:



$$\Delta E_1 = E_{(ZnO+Al_2O_3+Zn\text{-monolayer})} - [E_{(Al_2O_3+ZnO)} + n\mu_{Zn}], \quad (7)$$

$$\Delta E_2 = E_{(ZnO+Al_2O_3+O\text{-monolayer})} - [E_{(Al_2O_3+ZnO)} + n\mu_O], \quad (8)$$

for oxygen in gas phase  $\mu_O = \mu_{O_2}/2$ , while  $\mu_{Zn}^0 \leq \mu_{Zn} \leq \mu_{Zn}^{at}$  may be varied between the free atom value and the value corresponding to the bulk metal. Thus the chemical potential of Zn depends on the growth conditions and may be changeable in some limits. Table 3 represents the energy gain when an additional monolayer is inserted between substrate and grown ZnO film.

Results presented in table 3 show that in all cases there is a noticeable energy gain when both Zn- and O-type monolayers are introduced at the interface as compared to the case when these atoms are placed in the corresponding reservoirs. This result suggests that such a monolayer is thermodynamically stable and therefore one cannot correctly describe interface energetics when the monolayer is not included in the interface structure. However these results must be regarded only as illustrative and qualitative ones because an optimal number of atoms in the monolayer is still unknown and specific investigation is needed. In table 3, the number of atoms in monolayer was chosen to be equal to the number of corresponding atoms on the surface of slab. E.g. we suppose that the number of O atoms in the monolayer must be equal to the number of Zn atoms on the Zn-faced surface of ZnO and vice versa. In addition, the possibility of the existence of some mixture of Zn and O atoms in the monolayer must be considered in rigorous calculations as well. Nevertheless we believe that the location of the monolayer at the interface is proved in principle due to the sufficiently large values of energy gains shown in table 3.

Therefore the location of O- or Zn-monolayers at the interface corresponds to thermodynamic equilibrium and must manifest itself in certain conditions, e.g. at a relatively low temperatures at the initial stage of the ZnO/ $Al_2O_3$  growth process. Therefore it is worth considering the growth technique suggested in [12]. In this work the purposeful deposition of a single O-monolayer on the sapphire (0001) surface was performed at 300 °C followed

**Table 4.** Adhesion energies  $E_{\text{adh}}$  calculated for various interface structures. For interfaces with a Zn-monolayer the lower values correspond to bulk metal values for  $\mu_{\text{Zn}}$ , and higher values correspond—to free atom chemical potential.

Atoms of monolayer	Termination of ZnO surface	ZnO slab	Figure	$E_{\text{adh}}$ ( $\text{eV}/\text{\AA}^2$ )
w/o	Zn	Rotated	8(b)	0.105
w/o	Zn	Unrotated	10(b)	0.139
w/o	O	Rotated	9(b)	0.126
w/o	O	Unrotated	11(b)	0.123
O	Zn	Rotated	8(a)	0.275
O	Zn	Unrotated	10(a)	0.268
Zn	O	Rotated	9(a)	0.334–0.459
Zn	O	Unrotated	11(a)	0.288–0.399

by short-time annealing and use of an atomic layer deposition technique with diethyl-zinc and nitrous oxide molecules as precursors for Zn and O, respectively. This method enables the elimination of structural defects in the film and greatly improves structural and optical properties of ZnO films [12].

Our calculations show that a Zn-monolayer may be formed on the ZnO/Al<sub>2</sub>O<sub>3</sub> interface as well due to considerable energy gain as is seen from table 3.

#### 4.3. Estimation of adhesion energies of ZnO on $\alpha$ -Al<sub>2</sub>O<sub>3</sub> for 30° rotated and unrotated species: role of monolayers at the interface

Figures 8–11 represented model systems (slabs) used in our calculations. In particular figures 8 and 9 correspond to a 30° in-plane rotation of the ZnO film relative to the  $\alpha$ -Al<sub>2</sub>O<sub>3</sub> substrate, while figures 10 and 11 correspond to the hexagon-on-hexagon growth. Inclusion of O- and Zn-monolayers into the interface is combined with using the Zn- and O-faced ZnO slabs, respectively. It is seen that some degree of ZnO film amorphization in the close vicinity of the interfaces may be found in all cases, though amorphization near O-monolayers is clearly larger. Nevertheless distortion of the ZnO wurtzite structure is localized mainly on the double layer closest to the interface, which is in line with the high quality of ZnO films obtained in practice.

Table 4 presents a comparison of adhesion energies for interfaces with monolayers (both Zn- and O-containing) in the case of 30° rotated and unrotated ZnO films on the Al<sub>2</sub>O<sub>3</sub> substrate.

It is worth noting that there is one specific factor which limits the accuracy of calculations in the framework of the proposed model. Indeed, the calculated interfacial structure shows amorphous-like behaviour. Thus one may expect the existence of a number of local minima when the ZnO slab is slid along the Al<sub>2</sub>O<sub>3</sub> surface to get different interface structures (similar to the procedure proposed in [52]). Rigorously speaking, one must calculate the potential energy surface on a two-dimensional grid to be sure that the global minimum is obtained. We expect that the larger the surface supercell used, the more important this issue becomes. In our concrete case we deal with slabs of up to 460 atoms, for which several hundred steps are necessary for full geometry optimization. Thus such bulk calculations are awkward. Nevertheless we made some estimate for the rotated ZnO film for which a 192-atom slab was used. In this case we performed calculations in three different positions of the ZnO slab with respect to the Al<sub>2</sub>O<sub>3</sub> one. It appears that variation of energy subject to variation of the mutual slab positions is about 1.5 eV. Based on this estimate we believe that absolute errors in table 4 due to the above-mentioned effect may be as large as several hundredths (in  $\text{eV}/\text{\AA}^2$  units). Thus data from table 4 must be handled with care when the corresponding energies are relatively close to one another. Keeping in mind these qualifications and based on data presented in table 4 we may draw the following conclusions:

- A number of interface structures have noticeable adhesion energies and thus, in principle, may be realized in practice depending on the growth conditions.
- Inclusion of both O- or Zn-monolayers into the ZnO/Al<sub>2</sub>O<sub>3</sub> interface structure leads to a substantial increase in adhesion energies.
- Calculations do not give unique answer to the question of what kind of domains (unrotated or 30° rotated) are energetically preferable. Indeed, calculated differences between the adhesion energies of such domains are rather small and are of the same order of magnitude as the uncertainties in total energy calculation of slabs in a simulated interface which are estimated above. This is in line with numerous experimental observations [10–12, 53, 54] that both rotated and unrotated domains may coexist or one may prevail one over another depending on the experimental conditions.

## 5. Conclusion

ZnO and  $Zn_{1-x}Mn_xO$  films were grown on (0001) sapphire substrate by plasma-assisted molecular beam epitaxy at temperature  $T_s = 560^\circ\text{C}$ . X-ray, electronic and optical structural studies have shown that films have a single crystalline columnar structure with more unevenly distributed impurities and defects at the interfaces of columns. Both the ZnO and the  $Zn_{1-x}Mn_xO$  films have a hexagonal crystal structure of high quality with the ZnO hexagonal cell rotated by  $30^\circ$  relative to the sapphire substrate. Only ZnO wurtzite bands have been recorded for  $Zn_{1-x}Mn_xO$  films in XRD and micro-Raman spectra, while the presence of other secondary structural phases such as MnO,  $MnO_2$ ,  $Mn_3O_4$  or  $Zn_xMn_{3-x}O_4$  was not detected.

The presence of intense bands in the region of  $500\text{--}550\text{ cm}^{-1}$  in the Raman spectra of  $Zn_{1-x}Mn_xO$  films shows that Mn is embedded in a hexagonal lattice of ZnO. Despite their columnar structure, ZnO and  $Zn_{1-x}Mn_xO$  films have very high crystalline quality, as indicated by the small FWHM of the (0002) line in  $2\theta$  XRD spectra and small FWHM of  $E_2^{\text{low}}$  and  $E_2^{\text{high}}$  phonon bands in the Raman spectra. Evaluation of the lateral coherence length obtained from x-ray analysis of  $Zn_{1-x}Mn_xO$  films give values of  $\sim 900\text{--}400\text{ nm}$  which corresponds to an average column diameter. On the other hand coherent phonon length derived from the Raman spectra is  $\sim 36\text{--}10\text{ nm}$ , which is much smaller than a diameter of the hexagonal  $Zn_{1-x}Mn_xO$  columns. For 2D growth with screw dislocation density  $> 10^{10}\text{ cm}^{-1}$  the coherent phonon length corresponds to the alloy fluctuations of Mn in a single crystalline column of Mn-doped films. This suggests that damping of phonons is associated with a significant increase in the defect concentration at the column boundaries.

First-principle density functional calculations were performed to understand the structural and energetic characteristics of the ZnO/ $Al_2O_3$  interface. The difficulties in performing such calculations are caused by a large lattice mismatch between ZnO and sapphire structures. This leads to the necessity of using the model systems (slabs) represented by supercells with as many as 460 atoms with amorphous structure in the vicinity of the interface, which in turn leads to bulk computations.

In the present work we have considered various variants of ZnO/ $Al_2O_3$  interface structures. Namely, calculations were performed for both O-faced and Zn-faced ZnO surfaces. Based on calculations we predict the existence of O- and Zn-monolayers at the interface for Zn- and O-faced surfaces, respectively. Such structures are energetically preferable and lead to greater stability of the ZnO/sapphire interface. In all cases amorphization of the crystal structure in the vicinity of the interface appears as a natural result of calculations leading to reduction of internal strains originating from the ZnO/ $Al_2O_3$  lattice mismatch.

An essential part of the work is devoted to clarification of the nature of ZnO domains rotated by  $30^\circ$  with respect to sapphire substrates. It appears that the energy states for the system ZnO/sapphire with rotated and unrotated hexagonal cells are not very different, as is shown in table 4. Nevertheless, one may conclude that growth of  $30^\circ$ -rotated domains is somewhat preferred. These conclusions are in line with numerous experiments where both types of domains may be observed depending on the growth conditions.

We note that in the case of a Zn-monolayer which combines with an O-faced ZnO surface the adhesion energy possess the maximum value of  $0.334\text{--}0.459\text{ eV}/\text{\AA}^2$  depending on the chemical potential of the Zn atoms, which is specific to each concrete growth method.

The most energetically profitable interface configuration obtained when Zn-monolayer is placed between the (0001) sapphire surface and ZnO film can facilitate the process of doping with Mn atoms. Since the ionic radii of  $Zn^{2+}$  and  $Mn^{2+}$  are close to each other, Mn atoms must substitute for Zn in ZnO films. This suggests that grown  $Zn_{1-x}Mn_xO$  films may contain a significant number of Mn atoms at the interface, which may be responsible for reducing the size of grains in  $Zn_{1-x}Mn_xO$  films with increasing concentrations of Mn.

Finally, we note that the present calculations were performed under the assumption that the ZnO film lattice parameter accommodates to the lattice parameter of the sapphire substrate. However, it is obvious that such accommodation is possible only for sufficiently thin films, while for thicker films the energy will rise due to the appearance of large strains, which compensate for the energy gain due to the creation of new chemical bonds at the interface. In the case of a rotated ZnO domain, the energy rise is caused by the film thickness, and the related appearance of stretching strain leads to effective film contraction in the lateral direction, which manifests itself by the column-like film structures observed experimentally [12]. In this way, stretching strains inherent for rotating domains are eliminated.

In conclusion, we note a number of unresolved problems concerning the behaviour of Mn in doped ZnO films. Namely, the differences in the structure and concentration of Mn-related centers located at the interface compared with the ones in the bulk-like regions of the film are still unknown. One may expect such differences to be sufficient due to the interaction of Mn with monolayer atoms, with intrinsic defects specific for an interface and due to the creation of small Mn complexes in the interface region.

## References

- [1] Lerong F 2012 *12th Int. Workshop on Junction Technology (IWJT)* 53–6
- [2] Yoshida H and Sato K Circular polarization spin semiconductor laser using magnetic semiconductor and laser beam generating method *US Patent Specification*
- [3] Benzid K, Chetoui A, Maamache M, Turek P and Tribollet J 2013 *Europhys. Lett.* **104** 47005
- [4] Yang Y C, Pan F and Zeng F 2010 *New J. Phys.* **12** 023008
- [5] Kim H-J, Sim J-H, Kim H-J, Hong S-K, Kim D-J, Ihm Y-E and Choo W-K 2005 *J. Magn.* **10** 95
- [6] Archer P I and Gamelin D R 2006 *J. Appl. Phys.* **99** 08M107
- [7] Ohkubo I, Ohtomo A, Ohnishi T, Mastumoto Y, Koinuma H and Kawasaki M 1999 *Surf. Sci.* **443** L1043
- [8] Kim S S, Moon J H, Lee B-T, Song O S and Je J H 2004 *J. Appl. Phys.* **95** 454
- [9] Mandal S K and Nath T K 2006 *Thin Solid Films* **515** 2535
- [10] Liu C, Chang S H, Noh T W, Abouzaid M, Ruterana P, Lee H H, Kim D W and Chung J S 2007 *Appl. Phys. Lett.* **90** 011906
- [11] Liu K-P, Yen K-Y, Lin P-Y, Gong J-R, Wu K-D and Chen W-L 2011 *J. Vac. Sci. Technol. A* **29** 03A101
- [12] Lin Y-T, Chung P-H, Su H-L, Lai H-W, Lyu D-Y, Yen K-Y, Lin T-Y, Kung C-Y and Gong J-R 2009 *Appl. Surf. Sci.* **256** 819
- [13] Deparis C, Morhain C, Zuñiga-Pérez J, Chauveau J-M, Kim-Chauveau H, Vennéguès P, Teisseire M and Vinter B 2013 *Phys. Status Solidi C* **10** 1322
- [14] Vézian S, Natali F, Semond F and Massies J 2004 *Phys. Rev. B* **69** 125329
- [15] (Berlin: Springer) 94
- [16] Li Y F et al 2007 *Appl. Phys. Lett.* **91** 021915
- [17] Water W and Chu S Y 2002 *Mater. Lett.* **55** 67
- [18] Feng Z C (ed) 2012 (*Handbook of Zinc Oxide and Related Materials* vol 2) (Boca Raton, FL: CRC Press) 94
- [19] Vigué F, Vennéguès P, Deparis C, Vézian S, Laügt M and Faurie J-P 2001 *J. Appl. Phys.* **90** 5115
- [20] Wallis D J, Zhu D, Oehler F, Westwater S P, Pujol A and Humphreys C J 2013 *Semicond. Sci. Technol.* **28** 094006
- [21] Stanchu H, Kladko V, Kuchuk A V, Safriuk N, Belyaev A, Wierzbicka A, Sobanska M, Klošek K and Zytikiewicz Z R 2015 *Nanoscale Res. Lett.* **10** 51
- [22] Kuchuk A V, Stanchu H V, Chen Li, Ware M E, Mazur Yu I, Kladko V P, Belyaev A E and Salamo G J 2014 *J. Appl. Phys.* **116** 224302
- [23] Han H 2013 *Commun. Theor. Phys.* **59** 751
- [24] Hanada T 2009 Basic properties of ZnO, GaN, and related materials *Oxide and Nitride Semiconductors Processing, Properties and Applications* ed T Yao and S-K Hong (Berlin: Springer)
- [25] Özgür Ü, Alivov Y I, Liu C, Teke A, Reshchikov M A, Dogan S, Avrutin V, Cho S-J and Morkoç H 2005 *J. Appl. Phys.* **98** 041301
- [26] *Landolt-Bornstein New Series Group III* vol 17a (Berlin: Springer) 45
- [27] Safriuk N V, Stanchu G V, Kuchuk A V, Kladko V P, Belyaev A E and Machulin V F 2013 *Semicond. Phys. Quantum Electron. Optoelectron.* **16** 265
- [28] Metzger T, Hepler R and Born E 1998 *Phil. Mag.* **77** 1013
- [29] Cuscó R, Alarcón-Lladó E, Ibáñez J, Artú L, Jiménez J, Wang B and Callahan M J 2007 *Phys. Rev. B* **75** 165202
- [30] Serrano J, Romero A H, Manjón F J, Lauck R, Cardona M and Rubio A 2004 *Phys. Rev. B* **69** 094306
- [31] Callender R, Sussman S, Selders M and Chang R 1973 *Phys. Rev. B* **7** 3788
- [32] Samanta K, Bhattacharya P, Katiyar R S, Iwamoto W, Pagliuso P G and Rettori C 2006 *Phys. Rev. B* **73** 245213
- [33] Šćepanović M, Grujić-Brojčin M, Vojisavljević K, Bernik S and Srećković T 2010 *J. Raman Spectrosc.* **41** 914
- [34] Fonoberov V A and Balandin A A 2004 *Phys. Rev. B* **70** 233205
- [35] Strelchuk V V, Bryksa V P, Avramenko K A, Lytvyn P M, Ya V M, Pashchenko V O, Bludov O M, Deparis C, Morhain C and Tronc P 2011 *Semicond. Phys. Quantum Electron. Optoelectron.* **14** 31
- [36] Phan T-L, Yu S C, Vincent R, Bui H M, Thanh T D, Lam V D and Lee Y P 2010 *J. Appl. Phys.* **108** 044910
- [37] Hadžić B, Romčević M, Kuryliszyn-Kudelska I, Dobrowolski W, Wróbel R, Narkiewicz U and Sibera D 2014 *J. Alloys Compd.* **585** 214
- [38] Richter H, Wang Z P and Ley L 1981 *Solid State Commun.* **39** 625
- [39] Campbel I H and Fauchet P M 1984 *Solid State Commun.* **58** 739
- [40] Kosacki Suzuki T, Anderson Harlan U and Colomban P 2002 *Solid State Ion.* **149** 99
- [41] Serrano J, Widulle F, Romero A H, Rubio A, Lauck R and Cardona M 2003 *Phys. Status Solidi B* **235** 260
- [42] Li H, Zhang W and Smith J R 2011 *Phys. Status Solidi A* **208** 1166
- [43] Wang X-G and Smith J 2005 *Phys. Rev. Lett.* **95** 156102
- [44] Du X L, Murakami M, Iwaki H and Yoshikawa A 2002 *Phys. Status Solidi A* **192** 183
- [45] Ordejón P, Artacho E and Soler J M 1996 *Phys. Rev. B* **53** R10441
- [46] Soler J M, Artacho E, Gale J D, García A, Junquera J, Ordejón P and Sánchez-Portal D 2002 *J. Phys. Condens. Matter* **14** 2745
- [47] Perdew J P, Burke K and Ernzerhof M 1996 *Phys. Rev. Lett.* **77** 3865
- [48] Monkhorst H J and Pack J D 1976 *Phys. Rev. B* **13** 5188
- [49] Troullier N and Martins J L 1991 *Phys. Rev. B* **43** 1993
- [50] Kresse G and Furthmüller J 1996 *Comput. Mater. Sci.* **6** 15
- [51] Soares E A, Van Hove M A, Walters C F and McCarty K F 2002 *Phys. Rev. B* **65** 195405
- [52] Feng J, Zhang W and Jiang W 2005 *Phys. Rev. B* **72** 115423
- [53] Wang C M, Saraf L V, Hubler T L and Nachimuthu P 2008 *J. Mater. Res.* **23** 13
- [54] Du X, Murakami M, Iwaki H, Ishitani Y and Yoshikawa A 2002 *Japan. J. Appl. Phys.* **41** L1043